ACS APPLIED MATERIALS & INTERFACES

www.acsami.org

Research Article

Self-Assembly of Precisely Fluorinated Albumin for Dual Imaging-Guided Synergistic Chemo−Photothermal−Photodynamic Cancer Therapy

Lijun Zhu, Yu Li, Mou Jiang, Changsheng Ke, Hanxiong Long, Maosong Qiu, Lei Zhang, Chaohui Ye, Xin Zhou, Zhong-Xing Jiang,* and Shizhen Chen*

Cite This: *ACS Appl. Mater. Interfaces* 2023, 15, 2665−2678

Read Online

ACCESS | Metrics & More | Article Recommendations | Supporting Information

ABSTRACT: Although albumin has been extensively used in nanomedicine, it is still challenging to fluorinate albumin into fluorine-19 magnetic resonance imaging (^{19}F MRI)-traceable theranostics because existing strategies lead to severe ^{19}F signal splitting, line broadening, and low ^{19}F MRI sensitivity. To this end, 34-cysteine-selectively fluorinated bovine serum albumins (BSAs) with a sharp singlet ^{19}F peak have been developed as ^{19}F MRI-sensitive and self-assembled frameworks for cancer theranostics. It was found that fluorinated albumin with a non-binding fluorocarbon and a long linker is crucial for avoiding ^{19}F signal splitting and line broadening. With the fluorinated BSAs, paclitaxel (PTX) and IR-780 were self-assembled into stable, monodisperse, and multifunctional nanoparticles in a framework-promoted self-emulsion way. The high tumor accumulation, efficient cancer cell uptake, and laser-triggered PTX sharp release of the BSA nanoparticles enabled ^{19}F MRI-near infrared fluorescence imaging (NIR FLI)-guided synergistic chemotherapy (Chemo), photothermal and photodynamic therapy of xenograft MCF-7 cancer with a high therapeutical index in mice. This study developed a rational synthesis of ^{19}F MRI-sensitive albumin and a framework-promoted self-emulsion of multifunctional BSA nanoparticles, which would promote the development of protein-based high-performance biomaterials for imaging, diagnosis, therapy, and beyond.

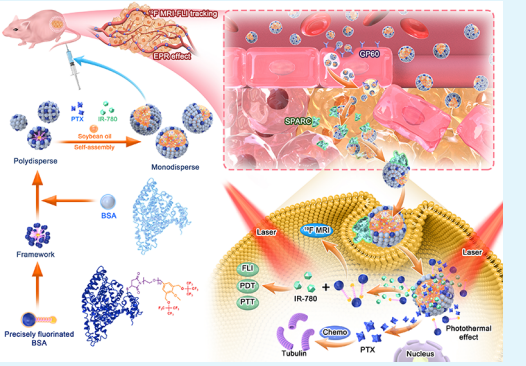

KEYWORDS: *albumin fluorinating, self-assemble nanoparticles, ^{19}F MRI, fluorescence, controlled release, photodynamic therapy*

1. INTRODUCTION

In recent years, albumin has become the most used protein in nanomedicine. Besides its abundance, long half-time, high biocompatibility, good biodegradability, and non-immunogenicity, albumin can escape from systemic clearance and degradation, accumulate in tumor regions, and be taken up and metabolized by cancer cells, which makes it an ideal drug delivery vehicles.[1−5] The approval of Abraxane led to overwhelming research on albumin nanoparticles.[6−8] Despite the diversity in nanostructures and components, there are two main strategies to develop albumin nanoparticles: physical absorption and covalent modification. Because of the weak interactions, albumin nanoparticles prepared through physical absorption are prone to dissociation and burst drug release under biological conditions.[9] Although covalent bonds can significantly improve stability, unspecific modification, conjugation, and crosslink are usually used to construct albumin nanoparticles, leading to heterogeneous components and nanostructures, severely altered albumin structures and biological properties, and possible immunogenicity and toxicity.[10−14] Thus, the development of albumin nanoparticles through precise covalent modification without crosslink and heterogeneity may maximize the benefits of albumin as a natural vehicle for cancer drug delivery.

Integrating multimodal imaging into albumin nanoparticles facilitates imaging-guided drug therapy with high therapeutical indexes.[15−17] ^{19}F MR-FL dual-modal imaging is highly attractive among the imaging modalities.[18−22] The low cost, high sensitivity, and high spatiotemporal resolution of FLI facilitate real-time monitoring of the targets, especially at the cellular level. Notably, albumin can bind many fluorophores and improve their optical performance,[23] providing a convenient way to construct fluorescent albumin nanoparticles. Because many FL agents, such as ICG, IR-780, and BODIPY, are also excellent photosensitizers for photothermal therapy (PTT) and photodynamic therapy (PDT), these fluorescent albumin nanoparticles are valuable in combined cancer

Received: October 24, 2022
Accepted: December 25, 2022
Published: January 5, 2023

Downloaded via INNOVATION ACAD PREC MSRMNT APM on February 3, 2023 at 01:07:12 (UTC).
See https://pubs.acs.org/sharingguidelines for options on how to legitimately share published articles.

ACS Publications © 2023 American Chemical Society

Scheme 1. Schematic Illustration of Versatile BSA Nanoparticles, Formed by Framework-Promoted Self-Emulsion of Fluorinated BSA, PTX, IR-780, and Soybean Oil, for ^{19}F MR-NIR FL Dual Imaging-Guided Synergistic Chemo−PTT−PDT of Cancer

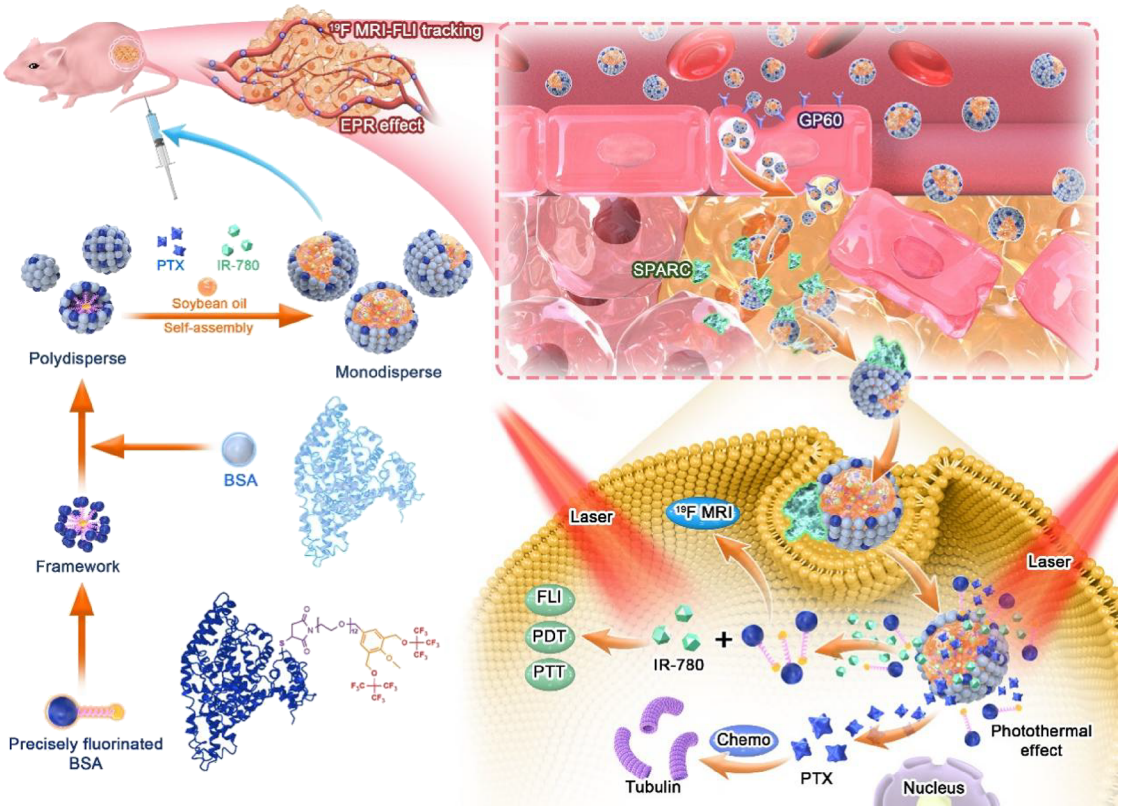

therapy.[24−26] However, the poor photon penetration depth limits the FLI of deep organs. To this end, NIR FLI has shown improved tissue penetration capability.[27−30] Moreover, ^{19}F MRI perfectly complements FLI by providing quantitative, background-free, and tissue depth limit-free "hot-spot" images.[31−36] Although many fluorinated albumin nanoparticles have been developed through noncovalent encapsulation of perfluorocarbons,[37−39] their ^{19}F MRI capability has seldom been explored. Notably, the high density, low intermolecular interactions, and ^{19}F signal splitting of perfluorocarbon often lead to low nanoparticle stability and ^{19}F MRI sensitivity. In contrast, covalent modification of albumin with fluorocarbons may significantly improve nanoparticle stability, shorten the relaxation times of ^{19}F, and thus improve the ^{19}F MRI sensitivity by reducing the data collection time. Therefore, it would be highly beneficial to covalently modify albumin with fluorocarbons for the construction of stable, ^{19}F MR-FL dual imaging traceable and multifunctional nanoparticles.

However, as far as we know, there are only a handful of reports on the covalent modification of albumins with fluorocarbons. Mehta et al. and Godovikova et al. trifluoroacylated the multiple surface amino groups on albumin,[40−43] while the resulting albumins showed split and broad ^{19}F signals, severely modifying the solubility and biological behaviors. Then, Yu et al. developed perfluoro-*tert*-butoxylated tags and selectively conjugated them to the 34-cysteine of albumin (Scheme 2),[44] which gave multiple broad ^{19}F NMR peaks with ultra-short transverse relaxation times, hindering their ^{19}F MRI application. The severe ^{19}F signal splitting and line broadening were probably caused by the short linkers and albumin binding of the fluorocarbon.[45−49] Therefore, precise modification of albumin with non-binding fluorocarbons through a long and flexible linker may deliver fluorinated albumin with high ^{19}F MRI sensitivity and preferred physicochemical properties.

Herein, we developed PTX- and IR-780-loaded BSA theranostics for ^{19}F MRI-FLI-guided synergistic Chemo−photothermal−photodynamic therapy of xenograft MCF-7 human breast cancer through precise fluorination of BSA and framework-promoted self-emulsion of BSA nanoparticles (Scheme 1). On the one hand, a series of fluorinated tags were designed with bulky hydrophobic fluorocarbon, flexible hydrophilic monodisperse oligoethylene glycols (M-OEGs) linkers, and thiol-reactive maleimide. In the fluorocarbon, two perfluoro-*tert*-butoxyl groups were symmetrically installed on the benzyl group to build up the size, prevent BSA binding, and thus improve the fluorine atoms' mobility. Therefore, the 18 chemically equivalent fluorine atoms would provide an intense ^{19}F NMR signal without signal splitting and line broadening for sensitive ^{19}F MRI. A series of M-OEG linkers were employed to accurately tune the mobility of the fluorocarbon and thus optimize the ^{19}F relaxation times for sensitive ^{19}F MRI. The maleimide-containing fluorinated tags were supposed to selectively conjugate BSA at the only free cysteine on the protein surface (34-cysteine), providing fluorinated BSAs with accurate structures. On the other hand, the fluorinated BSAs were amphiphilic and tended to aggregate into a framework with a fluorocarbon core and a BSA surface. Meanwhile, the maleimide non-reactive BSAs[50] in the systems would complement the nanostructure and deliver stable BSA nanoparticles with minimal BSA structural changes. Hydrophobic PTX and IR-780, the anticancer drug and NIR FL agent, respectively, would self-assemble in the hydrophobic

https://doi.org/10.1021/acsami.2c19161
ACS Appl. Mater. Interfaces 2023, 15, 2665−2678

Scheme 2. Synthesis of Fluorinated Tags 1a−1e and the Fluorinated Tags Developed by Yu et al.[44]

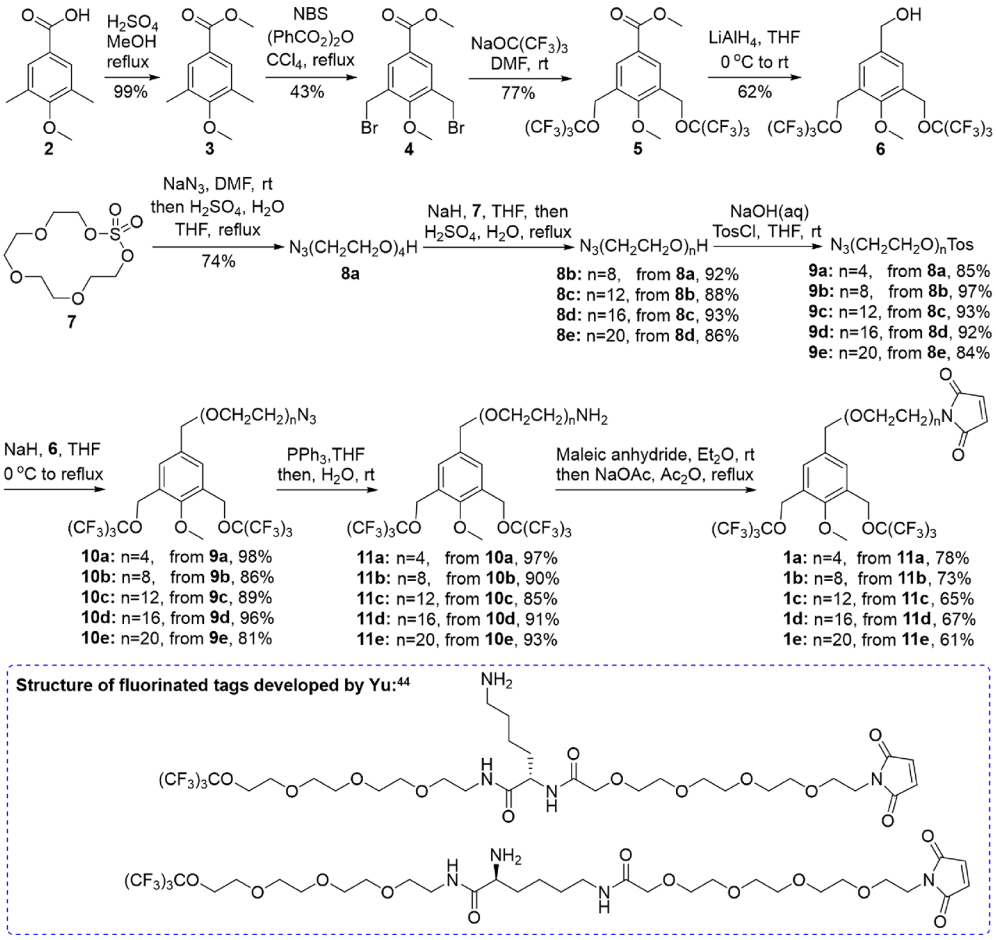

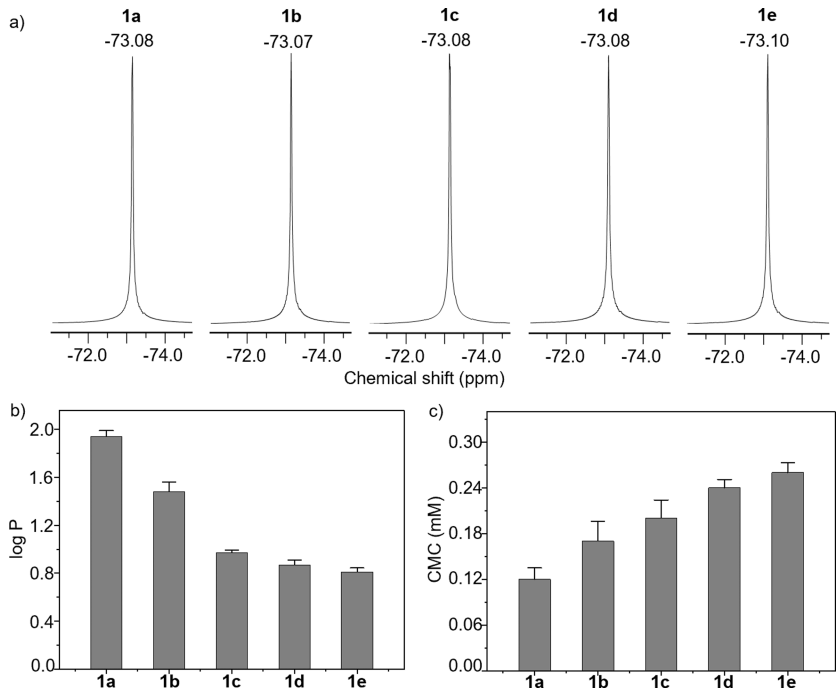

Figure 1. Partial ^{19}F NMR spectra (a, in $CDCl_3$), log P (b), and CMC (c) of fluorinated tags **1a−1e**.

core and BSA binding sites, further strengthening the hydrophobic interactions and improving the nanoparticle stability. Under laser irradiation, the encapsulated IR-780 would alter the conformation and stability of the nanoparticle

https://doi.org/10.1021/acsami.2c19161
ACS Appl. Mater. Interfaces 2023, 15, 2665−2678

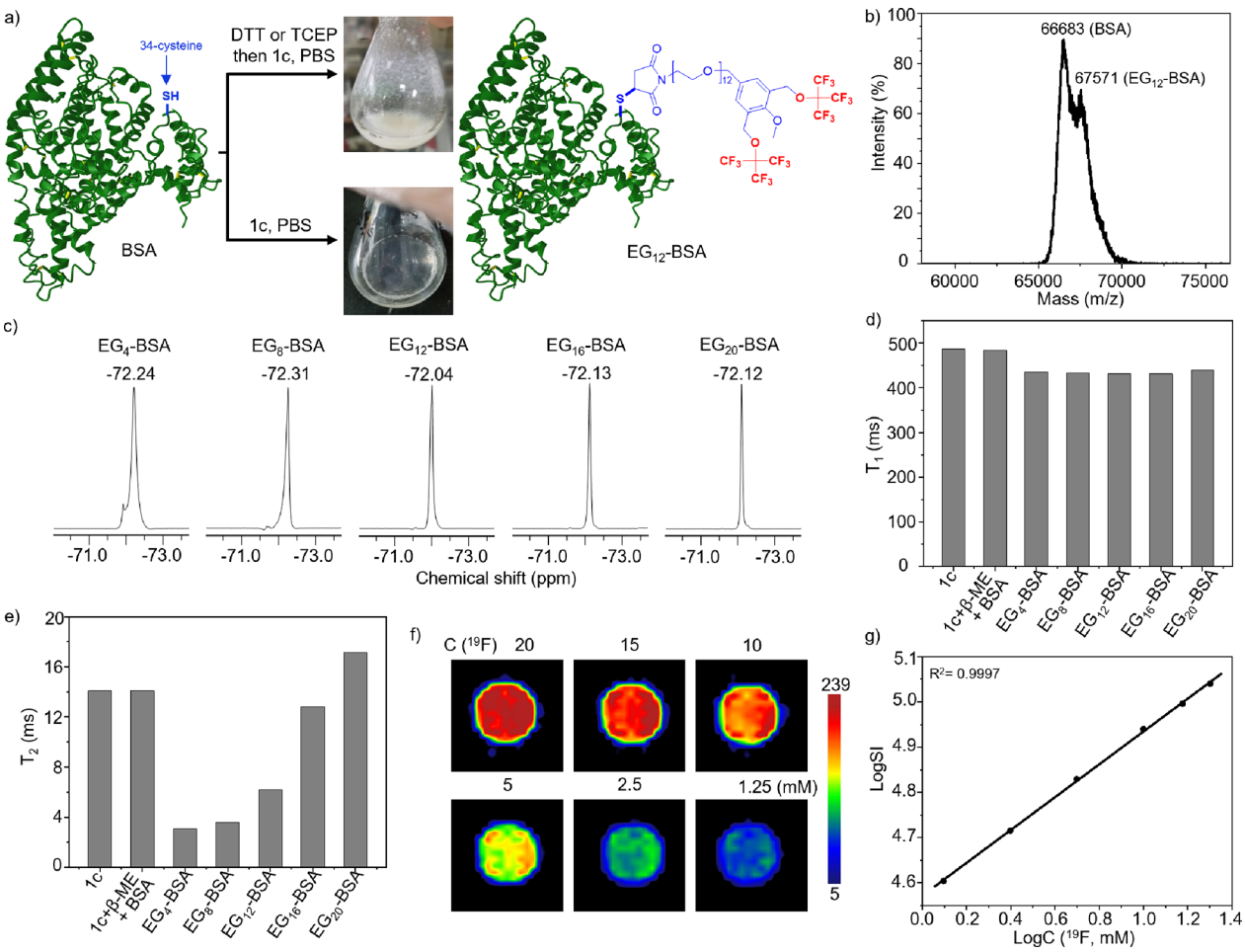

Figure 2. Schematic synthesis (a) and partial MALDI-TOF mass spectrum (b) of **EG$_{12}$-BSA**. Partial ^{19}F NMR spectra of fluorinated BSAs (c, in a mixture of H_2O and D_2O). ^{19}F T_1 (d) and T_2 (e) of fluorinated tag **1c**, a mixture of β-ME-blocked **1c** and BSA, and fluorinated BSAs at a ^{19}F concentration of 10 mM in a mixture of H_2O and D_2O. ^{19}F MRI phantom images (f) at the indicated ^{19}F concentrations and the logarithm plot of signal intensity (SI) versus ^{19}F concentration (g) of **EG$_{12}$-BSA**.

through the photothermal effect and generate reactive oxygens through the photodynamic effect, facilitating controlled PTX release and synergistic Chemo−PTT−PDT of cancer.

2. RESULTS AND DISCUSSION

2.1. Synthesis and Characterization of Fluorinated Tags. The synthesis of fluorinated tags **1a−1e** started with constructing fluorinated alcohol **6** (Scheme 2). After refluxing commercially available benzoic acid **2** in methanol with sulfuric acid as the catalyst, the resulting methyl ester **3** was then free-radically brominated with *N*-bromosuccinimide (NBS) in the presence of benzoyl peroxide to give dibromide **4** on a 7.3 g scale with 43% yield over two steps. Nucleophilic substitution of dibromide **4** with sodium perfluoro-*tert*-butoxide in *N*,*N*-dimethyl formaldehyde (DMF) gave fluorinated ester **5**,[35] which was reduced with lithium aluminum hydride to afford fluorinated alcohol **6** with a 48% yield over two steps. Then, a series of M-OEG azides **8a−8e** were prepared by sequentially nucleophilic ring-opening of tetraethylene glycol macrocyclic sulfate **7**,[51−53] which were then transformed into the corresponding tosylates **9a−9e**, respectively. Next, a highly efficient divergent synthesis of azides **10a−10e** was achieved by the Williamson ether synthesis between fluorinated alcohol **6** and tosylates **9a−9e**, respectively. After reducing azides **10a−10e** with triphenylphosphine and water, the corresponding amines **11a−11e** were treated with maleic anhydride and acetic anhydride to give fluorinated tags **1a−1e** with good yields, respectively. Over seven linear steps, fluorinated tags **1a−1e** were conveniently synthesized from acid **2** with high efficacy on multi-hundred-milligram scales.

Fluorinated tags **1a−1e** and their synthetic intermediates were fully characterized with ^{1}H/^{13}C/^{19}F NMR and mass spectra (see the Supporting Information). As expected, the symmetrical arrangement of two perfluoro-*tert*-butoxyl groups in fluorinated tags **1a−1e** provided an intense singlet ^{19}F NMR peak around −73.08 ppm (Figure 1a). Furthermore, a comparative study of fluorinated tags **1a−1e** was carried out to investigate the impact of M-OEG linker length on the physicochemical properties because considerable water solubility and self-assembly capability are crucial for downstream BSA conjugation and nanoparticle formulation. First, their lipophilicities were measured by the octanol−water partition coefficients (log P). It was found that the hydrophilic linker length played a vital role in log P, i.e., the longer the linker, the lower the log P, in which a 13.5-fold decrease in lipophilicity from **1a** to **1e** was found (Figure 1b). Second, the aggregation behaviors of the fluorinated tags were studied by measuring the critical micelle concentration (CMC). As expected, the increase in linker length considerably improved the hydrophilicity of the fluorinated tags and the corresponding CMCs

https://doi.org/10.1021/acsami.2c19161
ACS Appl. Mater. Interfaces 2023, 15, 2665−2678

increased from 0.12 mM (**1a**) to 0.26 mM (**1e**), a 2.2-fold increase (Figure 1c). Therefore, we precisely controlled the hydrophilic−hydrophobic balance and aggregation behaviors of fluorinated tags by accurately manipulating the M-OEG linker length, which may play an essential role in the physicochemical properties of fluorinated BSAs.

2.2. Synthesis and Characterization of Fluorinated BSAs. With fluorinated tags **1a**−**1e** in hand, their conjugation with BSA was carried out. As Ellman's assay on commercial BSA showed a free thiol content of 29.2%,[54] dithiothreitol (DTT) and tris(2-carboxyethyl)phosphine (TCEP) were employed to activate 34-cysteine. Unexpectedly, the reaction mixture of reduced BSA and fluorinated tag **1c** in phosphate-buffered saline (PBS) gradually turned into white jello (Figure 2a), showing the resulting fluorinated BSA's low water solubility. In contrast, direct conjugation of commercial BSA with fluorinated tag **1c** provided a transparent reaction mixture (Figure 2a). After Ellman's assay showed the completion of conjugation, the mixture was dialyzed to give a transparent mixture of non-reactive BSA and fluorinated BSA, named partially fluorinated BSA (**EG_{12}-BSA**). Based on the phenomena, we proposed a framework-promoted self-emulsion process during the conjugation: the hydrophobic fluorocarbons first aggregate into a hydrophobic core and drag the conjugated BSAs into a sparse surface, resulting in a fluorinated BSA framework. In the case of commercial BSA, non-reactive BSAs self-assemble onto frameworks and fill in the gaps on the surface to give water-soluble nanoparticles. In the case of reduced BSA, the hydrophobic fluorinated BSA frameworks would precipitate into jello without non-reactive BSAs to fill in the gaps on the surface. Thus, it is unnecessary to remove the non-reactive BSAs from the reaction mixture to construct BSA nanoparticles. Under the same conditions, BSA was conjugated with fluorinated tags **1a**, **1b**, **1d**, and **1e** to give the corresponding partially fluorinated BSAs **EG_4-BSA**, **EG_8-BSA**, **EG_{16}-BSA**, and **EG_{20}-BSA** as clear solutions.

Compared to our previous monodisperse polyethylene glycolated (M-PEGyated, M-PEG with an MW of 11,420 Da) BSAs,[55] the mass differences between fluorinated BSA and non-reactive BSA were minimal, which posed a challenge in isolating the fluorinated BSAs. Fortunately, the successful conjugation of fluorinated tags **1a**−**1e** to BSA was confirmed by MALDI-TOF mass and ^{19}F NMR spectra. Although the mass differences were relatively small, peaks of fluorinated BSAs were obvious at the right shoulder of non-reactive BSA peaks in MALDI-TOF mass spectra of the partially fluorinated BSAs (Figure 2b and Supporting Information). The conjugation was further confirmed by perfluoro-*tert*-butoxyl ^{19}F peak in the ^{19}F NMR spectra of the partially fluorinated BSAs after thorough dialysis (Figure 2c).

In contrast to the fluorinated BSAs in previous reports,[40−44] the partially fluorinated BSAs gave an intense, sharp, and singlet ^{19}F peak in water, except for **EG_4-BSA** (Figure 2c), which encouraged us to investigate the structure−^{19}F NMR relationship with ^{19}F relaxation times. First, the impact of linker length on the ^{19}F relaxation times was investigated. Longitudinal relaxation times (T_1) of about 440 ms for all the partially fluorinated BSAs indicated the neglectable effect of linker length on T_1 (Figure 2d), while their transverse relaxation times (T_2) dramatically increased with linker length from 3.07 ms of **EG_4-BSA** to 17.15 ms of **EG_{20}-BSA** (Figure 2e), indicating that short linkers may significantly restrict the mobility of fluorine atoms. Second, the fluorocarbon and BSA interactions were examined (Figure 2d,e). Compared to the relaxation times of fluorinated tag **1c** (T_1 = 487.1 ms, T_2 = 14.1 ms), considerable reductions were observed in the corresponding **EG_{12}-BSA** (T_1 = 441.9 ms, T_2 = 6.2 ms), while neglectable changes were observed in the mixture of mercaptoethanol (*β*-ME)-blocked **1c** and BSA (T_1 = 484.1 ms, T_2 = 14.1 ms). It is worth mentioning that **EG_{12}-BSA** displayed much shorter ^{19}F T_1 (441.9 vs 630.0 ms) and much longer ^{19}F T_2 (6.2 ms vs too short to be measured) than the fluorinated albumin reported by Yu and coworkers,[44] which is beneficial for ^{19}F MRI. Because T_2 of fluorinate compounds is highly sensitive to BSA binding,[48] the neglectable T_2 changes showed no apparent interaction between the bulky fluorocarbon and BSA. Third, the aggregation of the partially fluorinated BSAs in water was studied with dynamic light scattering (DLS). Surprisingly, the longer M-OEG linker led to smaller nanoparticles of partially fluorinated BSAs in water (Table 1, entries 1−5), indicating that the linker length also led to quite different frameworks of fluorinated BSAs, i.e., the shorter the linker, the more BSAs there are in a nanoparticle. Thus, besides modulating the mobility of the fluorine atoms in the fluorinated BSAs, the M-OEG linker length may also impact the relaxation times by tuning the nanoparticle size because large nanoparticles usually have short T_2 due to slow tumbling.[56] Because of its convenient synthesis and appropriate ^{19}F relaxation times, **EG_{12}-BSA** was chosen for the ^{19}F MRI phantom experiment, which was imaged at a low ^{19}F concentration of 1.25 mM with a data collection time of 10 min (Figure 2f). In contrast, the fluorinated BSAs developed by Yu and coworkers had too short ^{19}F T_2 to conduct the ^{19}F MRI phantom experiment.[44] Notably, the logarithm of **EG_{12}-BSA** signal intensity (SI) was proportional to the logarithm of the corresponding ^{19}F concentration, which facilitated the accurate quantification of fluorine concentration with ^{19}F MRI SI (Figure 2g). The ^{19}F concentration of **EG_{12}-BSA** was measured as 0.082 mmol/g (Figure S1). Therefore, we have developed **EG_{12}-BSA** with a strong and sharp ^{19}F peak as a sensitive and quantitative ^{19}F MRI agent by providing a relatively long M-OEG linker and building a bulky non-binding fluorocarbon, which would be a valuable strategy for developing ^{19}F MRI-traceable proteins.

Table 1. The Ingredients, Particle Sizes, PDIs, and Zeta Potentials of BSA Nanoparticles

entry	ingredients[a]	sizes[b] (PDI)	zeta potentials[c]
1	**EG_4-BSA**	117 (0.30)	−7.7
2	**EG_8-BSA**	76 (0.59)	−7.1
3	**EG_{12}-BSA**	40 (0.55)	−6.6
4	**EG_{16}-BSA**	30 (0.48)	−6.9
5	**EG_{20}-BSA**	25 (0.41)	−7.3
6	**EG_{12}-BSA**, PTX	85 (0.54)	−4.2
7	**EG_{12}-BSA**, PTX, soybean oil	141 (0.13)	−9.9
8	**EG_4-BSA**, PTX, soybean oil	151 (0.17)	−10.3
9	**EG_8-BSA**, PTX, soybean oil	146 (0.15)	−10.6
10	**EG_{16}-BSA**, PTX, soybean oil	145 (0.18)	−10.9
11	**EG_{20}-BSA**, PTX, soybean oil	147 (0.11)	−10.7
12	**EG_{12}-BSA**, PTX, soybean oil, IR-780	144 (0.11)	−9.6

[a]Amount of ingredients in 1 mL PBS: 20 mg of **EG_n-BSA**, 3 mg of PTX, 10 mg of soybean oil, and 0.8 mg of IR-780. [b]Size is the diameter in nm. [c]Zeta potential is given in millivolts.

https://doi.org/10.1021/acsami.2c19161
ACS Appl. Mater. Interfaces 2023, 15, 2665−2678

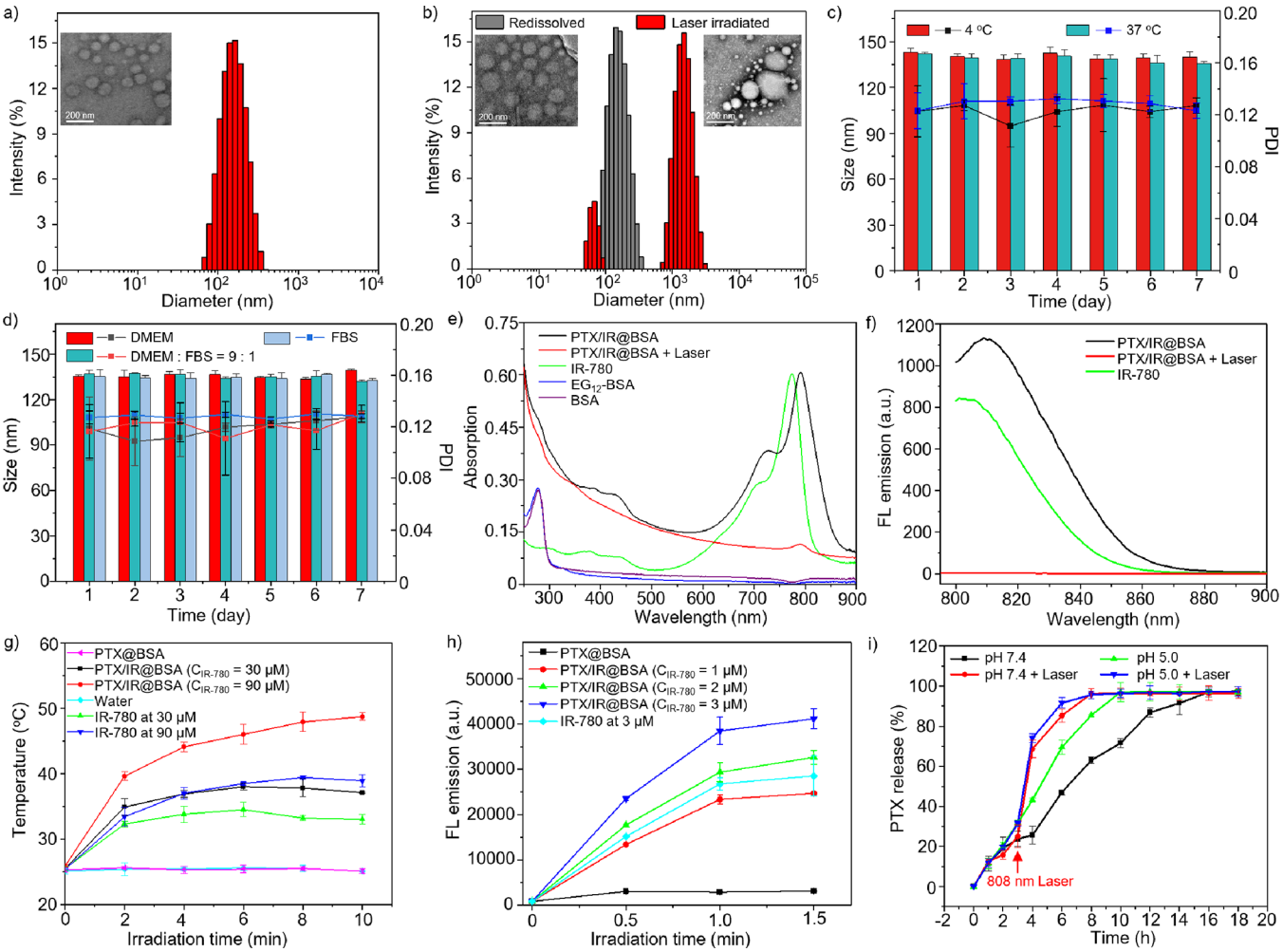

Figure 3. DLS and TEM images of **PTX/IR@BSA** (a: fresh, b: redissolved and after 5 min laser irradiation). Stability of **PTX/IR@BSA** at different temperatures (c) and in various mediums (d) monitored by DLS over 7 days. UV−vis absorption (e) and NIR FL emission (f) spectra of **PTX/IR@BSA** and IR-780. The plot of temperature elevation versus laser irradiation time (g) and SOSG FL emission spectra (h) of **PTX/IR@BSA** and IR-780 under laser irradiation. PTX release curves of **PTX/IR@BSA** under the indicated conditions (i). An 808 nm laser at 1 W cm^{-2} was used in all cases.

2.3. Formulation of Theranostics with Partially Fluorinated BSAs. With the preferred physicochemical properties, **EG_{12}-BSA** was employed to formulate theranostics for ^{19}F MR-NIR FL dual imaging-guided synergistic Chemo−PDT−PTT of cancer. Although it had self-emulsion capability (Table 1, entry 3), the direct formulation of PTX with **EG_{12}-BSA** gave polydisperse nanoparticles with a polydispersity index (PDI) of 0.54 (Table 1, entry 6). Then, soybean oil, a hydrophobic oil widely used in pharmaceutical formulation, was employed to dissolve the fluorocarbon and provide a hydrophobic core for better self-assembly of **EG_{12}-BSA**, i.e., creating monodisperse **EG_{12}-BSA** frameworks.[57] Fortunately, PTX-loaded **EG_{12}-BSA** nanoparticles, **PTX@BSA**, with a particle size of 141 nm and a low PDI of 0.13 were successfully prepared using a desolvation method (Table 1, entry 7). Interestingly, **PTX@BSA** (T_1 = 463.2 ms, T_2 = 11.8 ms) had a significantly longer T_2 than **EG_{12}-BSA** (T_1 = 441.9 ms, T_2 = 6.2 ms), confirming that soybean oil indeed dissolved the fluorocarbon and thus considerably improved the mobility of the fluorine atoms by eliminating the tangling of fluorocarbons. As a result, **PTX@BSA** was imaged at a low ^{19}F concentration of 1.25 mM with a data collection time of 37 min (Figure S4). Under the same conditions, a series of PTX-loaded BSA nanoparticles were prepared from the partially fluorinated BSAs (Table 1, entries 8−11). Notably, although the partially fluorinated BSA nanoparticles showed linker length-dependent particle sizes (Table 1, entries 1−5), the PTX-loaded BSA nanoparticles had quite similar particle sizes and PDIs (Table 1, entries 7−11), further confirming the dissolution of fluorocarbon in soybean oil. Based on these observations, we envision that the fluorocarbons are tangled in the partially fluorinated BSA nanoparticles, showing linker length-dependent particle sizes and relaxation times. Once the fluorocarbons are dissolved in soybean oil, the fluorocarbons are no longer tangled and, compared to the large soybean core, the relatively short linker length plays a neglectable role in the particle size of PTX-loaded BSA nanoparticles. Therefore, the soybean oil actually restructured the fluorinated BSA frameworks and promoted the self-emulsion of monodisperse BSA nanoparticles.

After adding IR-780, a highly monodisperse nanoparticle, **PTX/IR@BSA**, was formulated with a particle size of 144 nm and PDI of 0.11, PTX entrapment efficiency of 94% and loading content of 14%, and IR-780 entrapment efficiency of

https://doi.org/10.1021/acsami.2c19161
ACS Appl. Mater. Interfaces 2023, 15, 2665−2678

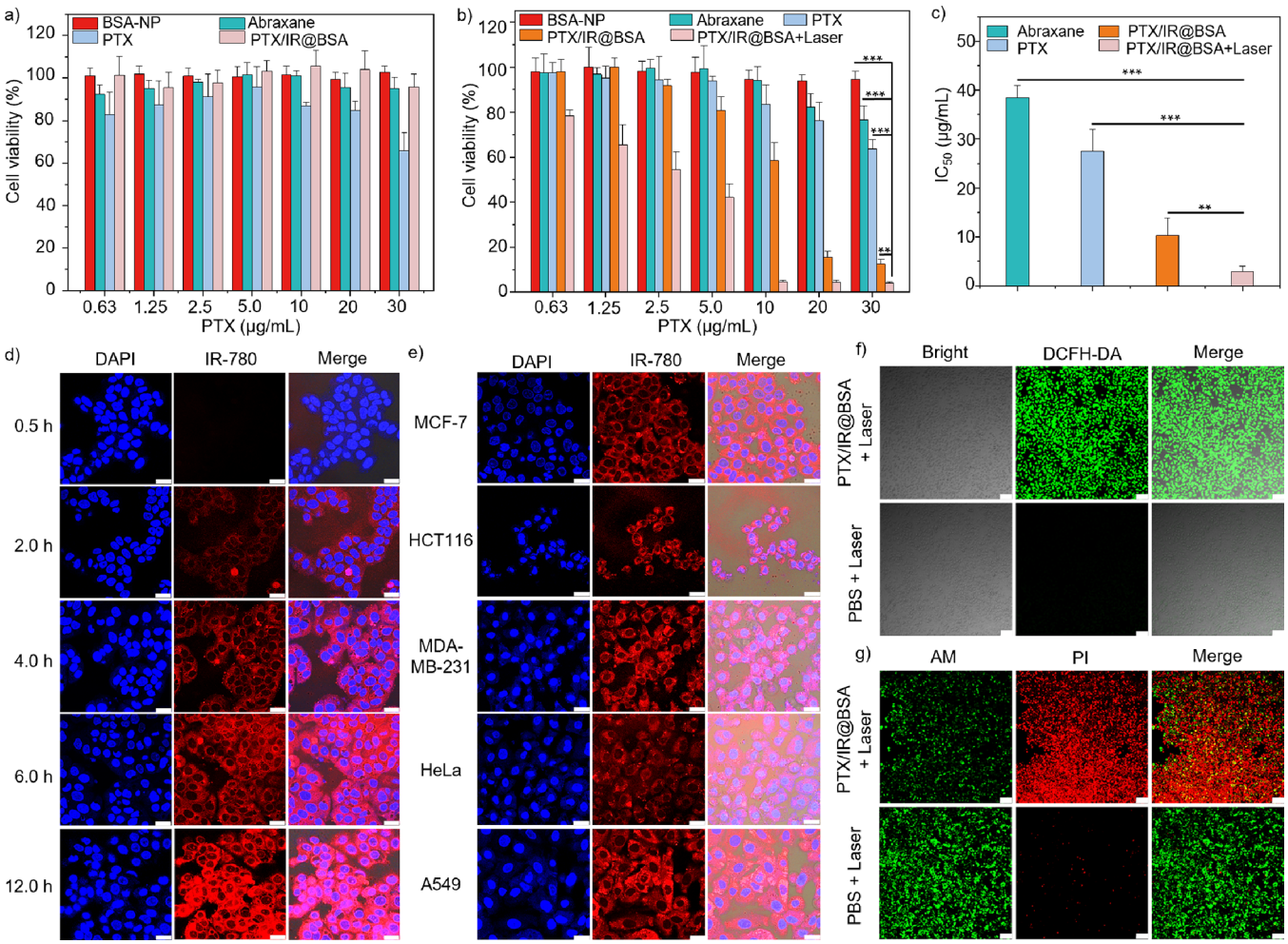

Figure 4. Biocompatibility assay in MCF-10A cells (a), cytotoxicity assay (b), and IC_{50} (c) in MCF-7 cells of **PTX/IR@BSA** with Abraxane, PTX, and **BSA-NP** as controls using CCK-8 assay. The confocal microscope images of **PTX/IR@BSA**-treated MCF-7 cells at a PTX concentration of 20 μg/mL at the indicated time points, scale bar: 25 μm (d). The confocal microscope images of MCF-7 cells, HCT-116 cells, MDA-MB-231 cells, HeLa cells, and A549 cells, scale bar: 25 μm (e) after 12 h of incubation. DCFH-DA-stained (f) and AM/PI double-stained (g) MCF-7 cells treated with **PTX/IR@BSA** and PBS after laser irradiation, scale bar: 100 μm. An 808 nm laser irradiation at 1 W cm^{-2} was used in all cases.

99% and loading content of 3% (Table 1, entry 12, Figure 3a). Moreover, the ^{19}F concentration of **PTX/IR@BSA** was measured as 0.051 mmol/g (Figure S1). Transmission electron microscopy (TEM) images further confirmed the particle size and monodispersity (Figure 3a). Notably, **PTX/IR@BSA** can be freeze-dried into green powder and redissolved in water with neglectable particle size and PDI changes (Figure 3b). Furthermore, **PTX/IR@BSA** showed high stability over 7 days toward temperature, cell culture medium, and fetal bovine serum (Figure 3c,d). Basically, the high monodispersity and stability and the freeze-drying and redissolving capability of **PTX/IR@BSA** are highly valuable for long-term storage and convenient use.

Next, the optical properties of **PTX/IR@BSA** were investigated. Compared to IR-780, **PTX/IR@BSA** had a red-shifted maximum NIR absorption at 789 nm and FL emission at 815 nm (Figure 3e,f), owing to the good dispersion of IR-780 in **PTX/IR@BSA** and the change in solvent polarity. After laser irradiation, the characteristic UV−Vis absorption and FL emission of **PTX/IR@BSA** almost disappeared due to laser-promoted nanoparticles and IR-780 degradation. At an IR-780 concentration of 90 μM, a temperature elevation of about 22.8 °C was observed in **PTX/IR@BSA** solution after an 808 nm laser irradiation of 10 min at 1 W cm^{-2}, which was 9.3 °C higher than IR-780 under the same conditions (Figure 3g). Benefiting from the red shift and broadening absorption of loaded IR-780, **PTX/IR@BSA** showed significant enhancement in the photothermal conversion efficiency (21.4 vs 12.7%) compared to IR-780. Using a singlet oxygen sensor green (SOSG) as the $^1O_2$ fluorescence probe, **PTX/IR@BSA** showed higher photodynamic efficacy than IR-780 under the same conditions (Figure 3h). Furthermore, the singlet oxygen species $^1O_2$ generation capability of **PTX/IR@BSA** was confirmed by the electron spin resonance (ESR) (Figure S3). Using a dialysis method to monitor the drug release, over 97% of PTX was released from **PTX/IR@BSA** in 16 h at pH 7.4 (Figure 3i). The drug release rate was accelerated under acidic conditions, with over 97% of PTX released in 10 h at pH 5.0. Furthermore, 808 nm laser irradiation of 5 min at the third hour dramatically accelerated the drug release at pH 7.4 and pH 5.0, with over 96% of PTX released in 8 h. Notably, the laser irradiation led to significant particle size and PDI expansions from 144 nm and 0.11 to 290 nm and 0.29, respectively (Figure 3b), indicating that the photothermal effect of IR-780 reassembled the nanostructure and dramatically accelerated the drug release. Therefore, the good

https://doi.org/10.1021/acsami.2c19161
ACS Appl. Mater. Interfaces 2023, 15, 2665−2678

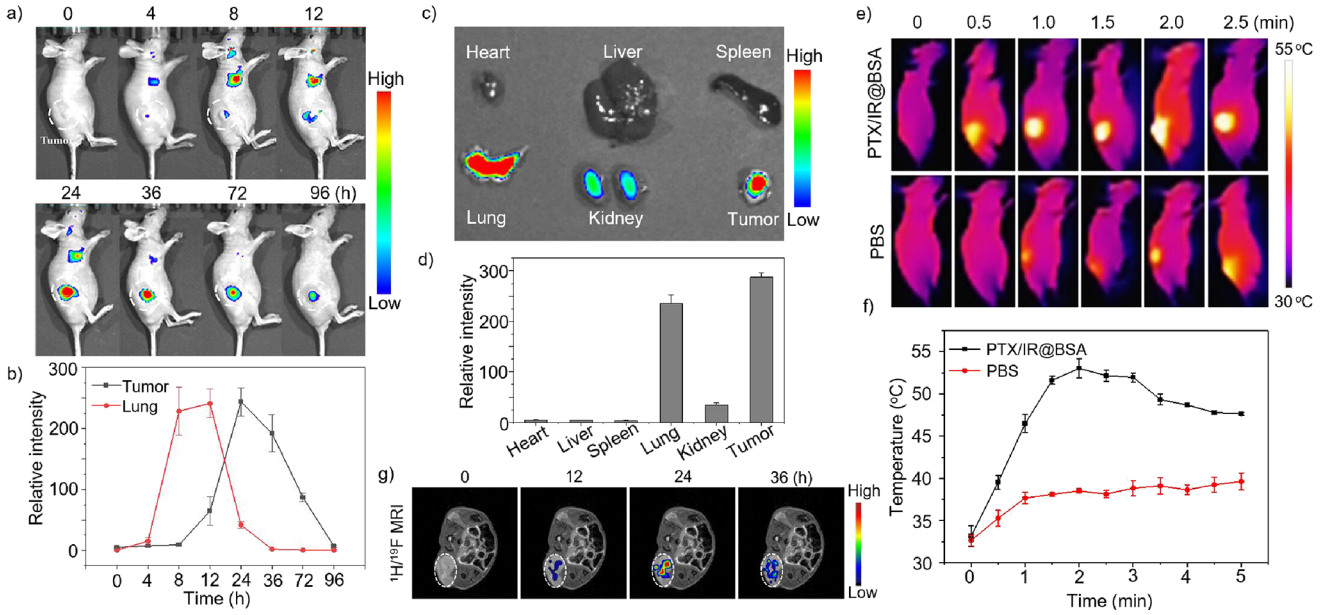

Figure 5. Whole-mouse NIR FL images (a), the plot of NIR FL intensities in lung and tumor regions versus time (b), NIR FL images (c), and intensities (d) of collected organs 24 h after injection of **PTX/IR@BSA**. Photothermal images (e) and the plot of tumor region temperature versus time (f) under 808 nm laser irradiation at 1 W cm^{-2} of mice 24 h after **PTX/IR@BSA** and PBS injection. IV injection of **PTX/IR@BSA** at 10 mg/kg of IR-780 was carried out on BALB/c nude mice. ^{19}F MRI of mice after IV injection (g) of **PTX/IR@BSA**. Groups of three mice were used in all cases.

encapsulation and dispersion of IR-780 in **PTX/IR@BSA** facilitated the red-shifted FL emission, high photothermal and photodynamic efficacies, and controlled PTX release.

2.4. Biocompatibility, Cytotoxicity, and Cell Uptake of PTX/IR@BSA. With **PTX/IR@BSA** in hand, its biocompatibility toward human breast epithelial MCF-10A cells and cytotoxicity toward human breast cancer MCF-7 cells were investigated using CCK-8 cytotoxicity assay. PTX, Abraxane, and PTX- and IR-780-free nanoparticle **BSA-NP** were used as controls. On the one hand, **PTX/IR@BSA** showed high biocompatibility of over 90% viability at a PTX concentration as high as 30 μg/mL, which was much higher than PTX and comparable to Abraxane (Figure 4a). Notably, no apparent cytotoxicity was found for **BSA-NP** with up to 200 μg/mL of **EG_{12}-BSA**. On the other hand, compared to Abraxane and PTX, **PTX/IR@BSA** showed significantly higher cytotoxicity toward MCF-7 cells, which was further improved after 3 min of 808 nm laser irradiation at 1 W cm^{-2} (Figure 4b). From the dose-responsive curves, the half-maximal inhibitory concentration (IC_{50}) of **PTX/IR@BSA** was calculated as 10.3 μg/mL, which was dramatically lower than those of Abraxane (38.4 μg/mL) and PTX (27.6 μg/mL, Figure 4c). Furthermore, the laser irradiation significantly lowered the IC_{50} of **PTX/IR@BSA** to 3.0 μg/mL, which was almost 13-fold higher than Abraxane.

The cell uptake of **PTX/IR@BSA** was then studied with laser confocal microscope images. The gradually increasing red NIR FL of IR-780 around the nucleus showed a significant uptake of **PTX/IR@BSA** in MCF-7 cells (Figure 4d). The merged FL images of IR-780 and nucleus dye DAPI indicated that **PTX/IR@BSA** remained in the cytoplasm after the uptake. Meanwhile, the uptake of **PTX/IR@BSA** was investigated in human colorectal cancer HCT-116 cells, triple-negative breast cancer MDA-MB-231 cells, cervical cancer HeLa cells, and lung cancer A549 cells. After 12 h of incubation, significant red FL of IR-780 in the cytoplasm of these cells showed high uptakes of **PTX/IR@BSA** (Figure 4e), indicating its broad potential for cancer therapy. Then, the reactive oxygen species (ROS) generation capability of **PTX/IR@BSA** was evaluated in MCF-7 cells using DCFH-DA as the fluorescence probe. After 6 h of incubation with **PTX/IR@BSA** and then 3 min of 808 nm laser irradiation at 1 W cm^{-2}, obvious green FL of DCFH-DA was detected in MCF-7 cells, while neglectable green FL was seen in PBS-treated MCF-7 cells (Figure 4f), indicating the high ROS generation ability of **PTX/IR@BSA** in cells. Finally, the PDT efficacy of **PTX/IR@BSA** was investigated using the AM-PI double staining in MCF-7 cells. The weak green FL of AM from live cells and strong red FL of PI from dead cells were observed in the **PTX/IR@BSA**-treated MCF-7 cells after 3 min of 808 nm laser irradiation at 1 W cm^{-2} (Figure 4g), showing the high PDT efficacy of **PTX/IR@BSA**. In contrast, only slight red FL of PI from dead cells was detected in PBS-treated MCF-7 cells after the laser irradiation.

Therefore, compared to Abraxane, **PTX/IR@BSA** showed high biocompatibility toward normal breast MCF-10A cells and nearly threefold higher cytotoxicity toward human breast cancer MCF-7 cells, which was further improved to almost 13-fold after the laser irradiation. On top of its high uptake by a series of human cancer cells, **PTX/IR@BSA** exhibited high ROS generation capability and PDT efficacy in cells for synergistic Chemo-PTT-PDT of cancer.

2.5. In Vivo NIR FLI, ^{19}F MRI, and Photothermal Efficacy of PTX/IR@BSA. In BALB/c nude mice, no acute toxicity was observed after intravenous (IV) injection of **PTX/IR@BSA** at a PTX concentration of 75 mg/kg. Then, the NIR FLI capability of **PTX/IR@BSA** was investigated in BALB/c nude mice carrying xenograft MCF-7 human breast tumors of about 200−300 mm^3. After IV injection, the whole-body NIR FLI showed that **PTX/IR@BSA** accumulated first in the lung region and then gradually in the tumor region (Figure 5a). The potential lung-targeting ability of BSA may account for the lung accumulation at the early stage.[58] In contrast, because the

https://doi.org/10.1021/acsami.2c19161
ACS Appl. Mater. Interfaces 2023, 15, 2665−2678

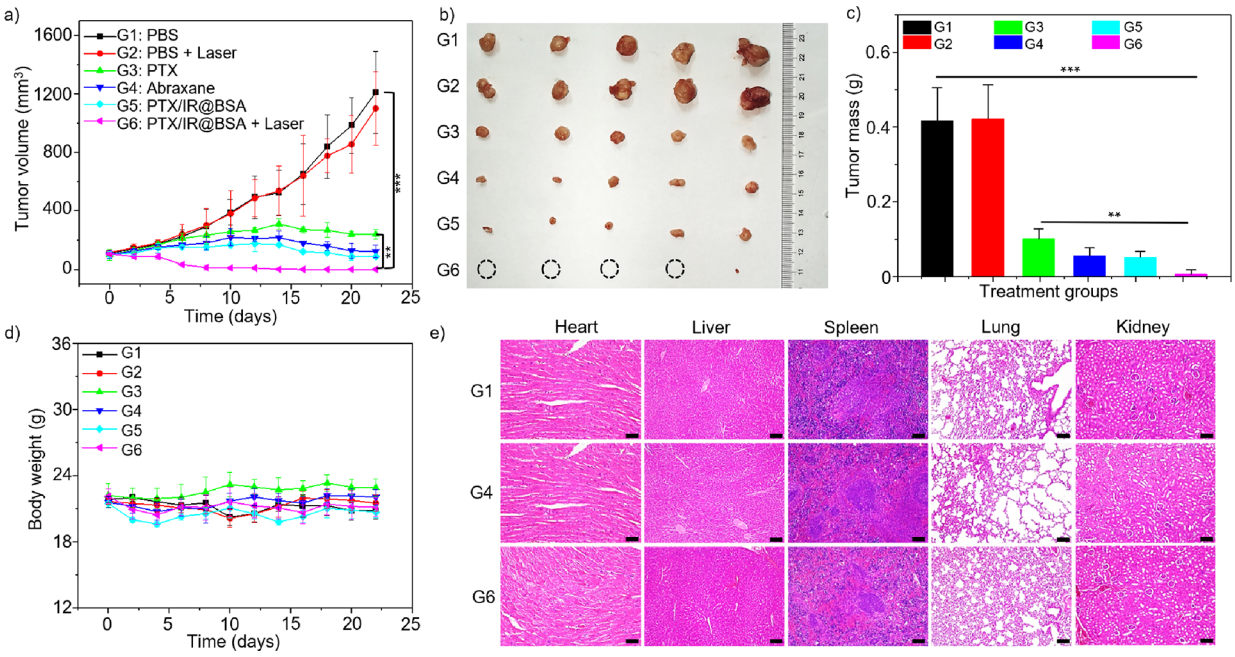

Figure 6. Tumor growth curves (a), tumor photos (b), tumor mass (c), and body weight curves (d) of six groups of mice treated with PBS (G1), PBS + laser (G2), PTX (G3), Abraxane (G4), **PTX/IR@BSA** (G5), and **PTX/IR@BSA** + laser (G6). H&E staining of internal organs from G1, G4, and G6 (e, the rest groups can be found in the Supporting Information), scale bar: 100 μm. Data were presented as mean ± standard deviation (n = 5, for a, c, d, the asterisks indicate the statistical significance between G6 and G1, G3, $^{**}p < 0.01$, and $^{***}p < 0.001$). Irradiation of 808 nm laser at 1 W cm^{-2} for 2 min at the tumor region 24 h after **PTX/IR@BSA** and PBS injection. Tumors and organs were collected on the 22nd day.

nanoparticles are not large enough (<2000 nm) to retain in the lungs,[59] **PTX/IR@BSA** gradually accumulate in the tumor region through the EPR effect and BSA-mediated tumor targeting. Quantitative analysis of the whole-body NIR FL images indicated that the peak NIR FL intensities in the lung and tumor regions were around the 8th and 24th hours, respectively (Figure 5b). A high NIR FL intensity in the tumor region was observed between the 12th and 72nd hours, which provided a long time window for NIR FL-guided synergistic Chemo−PTT−PDT of cancer. After sacrificing the mice, the NIR FL images (Figure 5c) and intensity analysis (Figure 5d) of collected internal organs confirmed a high accumulation of **PTX/IR@BSA** in the tumor and lungs, which also showed a slight accumulation in kidneys (Figure 5c,d). Interestingly, a neglectable NIR FL signal was observed in the heart, liver, and spleen, indicating the high tumor target of **PTX/IR@BSA**. The photothermal efficacy of **PTX/IR@BSA** was also investigated in MCF-7 tumor-carrying BALB/c nude mice using a thermal camera. After 2 min of laser irradiation, a significant temperature elevation of about 20 °C was detected in the tumor region (Figure 5e,f). In comparison, a slight temperature elevation in the tumor region was seen in the PBS-injected mice. Besides photothermally killing the cancer cells, the photothermal effect of **PTX/IR@BSA** may promote the selective in vivo PTX release in the tumor region for synergistic Chemo−PTT−PDT of cancer. Using a time-dependent in vivo ^{19}F MRI, the accumulation of **PTX/IR@BSA** in the tumor was observed 12 h after the intravenous injection (Figure 5g). Therefore, NIR FLI and ^{19}F MRI may guide the downstream synergistic Chemo−PTT−PDT of cancer by evaluating the drug targeting and estimating optimal laser irradiation time and drug dose frequency.

2.6. Synergistic Chemo−PTT−PDT of Xenograft MCF-7 Cancer with PTX/IR@BSA. With the high tumor accumulation and ^{19}F MR-NIR FL dual imaging capability, **PTX/IR@BSA** was employed in the imaging-guided synergistic Chemo−PTT−PDT of xenograft MCF-7 human breast cancer. When the tumor sizes reached about 100 mm^3, six groups of five BALB/c nude mice were IV injected with PBS (groups 1 and 2), PTX (group 3), Abraxane (group 4), and **PTX/IR@BSA** (groups 5 and 6) every 3 days, respectively. Compared to the PBS groups, a significant chemotherapy efficacy was observed in the PTX, Abraxane, and **PTX/IR@BSA** groups, while the highest tumor growth inhibition was observed in the **PTX/IR@BSA** groups (Figure 6a). The therapeutic efficacy of **PTX/IR@BSA** was further improved by 2 min of 808 nm laser irradiation with a power density of 1 W cm^{-2} at the 24th-hour post-injection (Figure 6a, group 6). After 21 days of therapy, the mice were sacrificed and the tumors were collected (Figure 6b). Notably, only a tiny tumor was collected from the five mice in group 6. Both tumor size and tumor mass analyses showed significant therapeutic efficacy in group 6 with $p < 0.01$ and 0.001 compared to the PTX and PBS groups, respectively (Figure 6a,c). No significant body weight loss was observed in the **PTX/IR@BSA** treatment groups during the therapy period (Figure 6d), indicating no apparent therapy-induced toxicity. Furthermore, no tissue damage was observed from the H&E staining of internal organs collected from the mice after the therapy (Figure 6e and Supporting Information). Obvious tissue damage was observed from the H&E staining of tumors collected from the **PTX/IR@BSA** treatment group (Supporting Information). The expressions of cell proliferation-related antigen Ki-67 were significantly downregulated in the tumor tissues receiving **PTX/IR@BSA**, indicating the suppressive effect of **PTX/IR@BSA** for inhibiting tumor growth (Supporting Information). Therefore, highly efficient ^{19}F MR-NIR FL dual imaging-guided synergistic Chemo−PTT−

https://doi.org/10.1021/acsami.2c19161
ACS Appl. Mater. Interfaces 2023, 15, 2665−2678

PDT of xenograft MCF-7 human breast cancer was achieved by **PTX/IR@BSA** without apparent toxicity.

3. CONCLUSIONS

Although albumin nanoparticles have been widely used in nanomedicine, novel strategies to develop high-performance albumin nanomaterials are precious. In this study, we have developed precisely fluorinated BSAs with sensitive ^{19}F MRI and self-assembly capabilities to construct monodisperse, stable, and multifunctional BSA nanoparticles for highly efficient ^{19}F MR-NIR FL dual imaging-guided synergistic Chemo−PTT−PDT of breast cancer. On the one hand, the rational synthesis has delivered the fluorinated BSA nanoparticles with high ^{19}F MRI sensitivity. First, the symmetrical assembly of perfluoro-*tert*-butanols into a bulky fluorocarbon not only provided an intense ^{19}F signal from 18 equivalent fluorine atoms but also avoided ^{19}F signal splitting by eliminating the interaction between fluorocarbon and BSA. Second, the relatively long, hydrophilic, and flexible M-OEG linkers were employed to improve the mobility of fluorocarbon and avoid the severe ^{19}F signal broadening. Third, dissolving hydrophobic fluorocarbon in soybean oil further enhanced the mobility of fluorocarbon and thus proved a sharp singlet ^{19}F peak. On the other hand, the self-assembly of fluorinated BSA delivered a framework for the self-emulsion of BSA, PTX, and IR-780 into nanoparticles with maximal retained physical and biological properties of albumin. The good dispersion of IR-780 and high loading of PTX in BSA nanoparticles enabled highly efficient ^{19}F MR-NIR FL dual imaging-guided synergistic Chemo−PTT−PDT of breast cancer on cell and mouse levels. Besides the high-performance fluorinated BSAs and BSA theranostics, this study developed valuable strategies for precise modification, tuning of the ^{19}F MRI sensitivity, and framework self-assembly of proteins, which would be highly important for engineering various proteins into multifunctional biomaterials of clinical potential. Nevertheless, the stability of hydrophobic interaction-based nanoparticles can be further improved by covalent bonds for more specific and sustained drug release, and the immunogenicity of the fluorinated BSA deserves examination for potential clinical application, which are under active study in this group and will be published in due course.

4. EXPERIMENTAL SECTION

4.1. Materials. Unless otherwise stated, all chemicals were obtained from commercial sources and used without further purification. All solvents were either analytical or HPLC grade. Deionized water was used unless otherwise indicated. Tetrahydrofuran (THF) and DMF were dried and freshly distilled prior to use. Reactions were monitored by thin layer chromatography (TLC) carried out on silica gel plates (HSGF254, Yantai Jiangyou), using iodine, $KMnO_4$, or a UV lamp for visualization. Purifications by silica gel chromatography were performed using silica gel (200−300 mesh) with petroleum ether (PE) and ethyl acetate (EA) or dichloromethane (DCM) and methanol. BSA was purchased from Life-iLab Biotech (Shanghai, China). Soybean oil medicinal grade was acquired from Aladdin (Shanghai, China). IR-780 iodide was purchased from J&K Scientific (Beijing, China). Paclitaxel was purchased from Accela (Beijing, China).

4.2. CMC and Log P of Compounds 1a−1e. The CMCs of compounds **1a−1e** were detected using pyrene as a fluorescent indicator (excitation wavelength, 334 nm). The ratio of fluorescence intensity at 384 and 373 nm from the pyrene was plotted against the compound concentration to calculate the CMC.

The log P of compounds **1a−1e** were measured using HPLC. An appropriate amount of the compound was dissolved in the water-saturated *n*-octanol to prepare solutions of a series of concentrations. The solution was analyzed by HPLC, and the standard curve was plotted from peak area values verse concentrations. A certain volume of the stock solution was mixed with an equal volume of *n*-octanol-saturated aqueous solution for 12 h. The organic phase was separated and subjected to HPLC quantitative analysis, and the compound concentration (C_o) in organic phase was calculated from the standard curve. Log P was then determined according to the formula log P = log $[C_o/(C_n-C_o)]$ (C_n represents the initial concentration; C_o represents the concentration of the organic phase), and the log P of each compound was obtained.

4.3. In Vitro ^{19}F MRI Study of Fluorinated BSAs. All ^{19}F MRI phantom experiments were performed on a 400 MHz Bruker BioSpec MRI system at 25 °C. Fluorinated BSA, EG_{12}-BSA, was serially diluted with PBS to give a series of the following ^{19}F concentrations: 20, 15, 10, 5, 2.5, and 1.25 mM. The ^{19}F density-weighted ^{19}F MRI phantom images were acquired by using a gradient-echo (GRE) pulse sequence, method = RARE, matrix size = 32 × 32, SI = 20 mm, FOV = 3.0 × 3.0 cm, TR = 4000 ms, TE = 3 ms, NS = 16, scan time = 600 s.

4.4. Preparation of Nanoparticles. To prepare **PTX/IR@BSA** nanoparticles, 15 mg of PTX, 4 mg of IR-780, and 50 mg of soybean oil were dissolved in 1 mL DCM. Then, 5 mL of 20 mg/mL fluorinated BSA solution was added. The dispersion was ultrasonicated at 250 W for 15 min, and the organic solvents were removed by rotary evaporation.

4.5. Characterization of Nanoparticles. DLS measurement was performed to determine the average particle size and zeta potential of nanoparticles using Malvern Zetasizer (Malvern, Nano ZS 90, UK). Data were given as mean ± standard deviation (SD) based on three independent measurements. TEM (Tecnai G20, FEI, USA, negative staining with phosphotungstic acid at 1%, w/v) was then used to further explore the morphology of nanoparticles.

Encapsulation efficiency (EE%) and drug loading efficiency (DLE %) of nanoparticles were determined using HPLC. Acetonitrile was added to the accurately weighed nanoparticles, then the mixture was sonicated for 30 min and centrifuged at 12,000 rpm for 10 min, and the supernatant was diluted to the corresponding concentration. The total content of PTX in nanoparticles (W_t) was determined by HPLC. Another equal amount of nanoparticles was dissolved in water, the mixture in the ultrafiltration centrifuge tube was centrifuged at 12,000 rpm for 10 min, and the filtrate was diluted to the corresponding concentration. The content of free PTX in nanoparticles (W_f) was determined by HPLC. The total weight of dried nanoparticles (W_d) was calculated, and EE% and DLE% were calculated as shown in eqs 1 and 2.

$$\mathrm{EE\%} = (W_t - W_f)/W_t \times 100\% \quad (1)$$

$$\mathrm{DLE\%} = (W_t - W_f)/W_d \times 100\% \quad (2)$$

The EE% and DLE% of IR-780 were measured in the same way.

4.6. Stability of PTX/IR@BSA. The nanoparticles were dispersed into PBS at 4 and 37 °C for 7 days or dispersed into DMEM, DMEM:FBS (9:1), and FBS for 7 days. The particle size and PDI were measured and recorded daily.

4.7. In Vitro Photothermal and Photodynamic Capability of PTX/IR@BSA. 1 mL samples were exposed to NIR laser irradiation (808 nm, 1 W cm^{-2}) for 5 min, and the temperature and image were obtained by an infrared thermal-imaging camera (Hikvision H13 Thermal Imager).

To explore the singlet oxygen generation capability, SOSG as a fluorescence sensor was added to the solutions of nanoparticles. After mixing well, the solution was exposed to NIR laser irradiation (808 nm, 1 W cm^{-2}) for a particular time period. The emission spectrum of SOSG was recorded to reflect the amount of singlet oxygen.

4.8. In Vitro Drug Release of PTX/IR@BSA. The PTX release behavior of nanoparticles was studied using the dialysis method. Specifically, 2 mL NP solution (2 mg/mL) was packed in a uniform

https://doi.org/10.1021/acsami.2c19161
ACS Appl. Mater. Interfaces 2023, 15, 2665−2678

pore dialysis bag (MWCO = 3.5 kDa) and fastened, then immersed in 30 mL PBS solution containing 0.2% (w/v) Tween-80 at different pH values (5.0, 7.4). The release system was then placed in a 37.5 °C thermostatic cradle and oscillated at a frequency of 100 rpm. Then, 1 mL PBS dialysate was collected at the predetermined time point and supplemented with 1 mL fresh PBS solution corresponding to the pH. After that, constant temperature oscillation dialysis was continued, and the content of PTX in each sample was calculated according to the above method for determining the paclitaxel content. The average value was obtained by measuring three times in parallel, and the time−drug cumulative release curve was plotted. Using the above method, under the condition of pH 7.4 and pH 5.0, laser irradiation (808 nm, 1 W cm^{-2}) was performed for 3 min after 3 h and the drug release was also measured.

4.9. Cell Experiments. MCF-7 cells seeded on a petri dish were cultured at 37 °C with 5% CO_2 for 24 h. Then, the cells were co-incubated with **PTX/IR@BSA** nanoparticles (IR-780 concentration: 5.4 μg/mL; PTX concentration: 20 μg/mL) for 6 h. After the treatment, the medium was removed and DCFH-DA was added at a concentration of 10^{-5} M. After incubation for 30 min, the cells were irradiated by NIR irradiation (808 nm, 1.0 W cm^{-2}, 3 min) and the intracellular singlet oxygen generation was observed using a confocal laser scanning microscopy (CLSM).

MCF-7 cells seeded on a petri dish were cultured at 37 °C with 5% CO_2 for 24 h. Then, the cells were co-incubated with drug-loaded nanoparticles (IR-780 concentration: 5.4 μg/mL; PTX concentration: 20 μg/mL) for 12 h. After the treatment, the medium was removed and refilled with a new medium. Then, the cells were irradiated by NIR irradiation (808 nm, 1 W cm^{-2}, 3 min). After incubating for 6 h, the medium was discarded. 1 μL of calcein AM (1000×) and PI (1000×) was diluted into 1 mL of detection buffer, respectively, to prepare the working solution. 1 mL of calcein AM/PI detection working solution was added to the confocal dish and incubated in the incubator for 30 min in the dark. Afterward, the cell-killing ability of drug-loaded nanoparticles was studied by CLSM.

MCF-7 cells were co-incubated with drug-loaded nanoparticles (IR-780 concentration: 5.4 μg/mL; PTX concentration: 20 μg/mL) at 37 °C for 0.5, 2, 4, 6, and 12 h, respectively. Afterward, the cellular uptake of drug-loaded nanoparticles was studied by CLSM. Fluorescent dye DAPI was used as the nucleus dye.

MCF-7 cells (5×10^3 cells per well) and MCF-10A cells (5×10^3 cells per well) were seeded in 96-well plates and incubated in 0.1 mL of DMEM containing 10% FBS at 37 °C in a humidified 5% CO_2 atmosphere for 24 h. After the culture medium was removed, 0.1 mL of fresh medium containing drug-loaded nanoparticles was added. After 12 h of incubation, the medium was removed and the cells were washed with PBS (pH 7.4) for three times and 0.1 mL of fresh medium was added. Then, the cells were illuminated using an 808 nm laser with an energy density of 1 W cm^{-2} for 3 min. For comparison, the cells without illumination were also studied. After 12 h of incubation, 0.1 mL of CCK-8 was added in each well. After incubation for 1 h, the optical density (OD) was measured at 450 nm using a microplate reader (Bio-Rad 550). Cell viability was calculated as follows: cell viability = $(OD_{treated}/OD_{control}) \times 100\%$, where $OD_{treated}$ was obtained from the cells after a particular treatment and $OD_{control}$ was obtained from the cells without treatment.

4.10. Animals and Tumor Model. The MCF-7 tumor model was established by subcutaneously injecting MCF-7 cells (1×10^7) suspended in 0.1 mL of PBS on the flank of the female BALB/c nude mouse.

4.11. In Vivo Biodistribution and Tumor Accumulation. When the tumor volume reached about 150 mm^3, the in vivo distribution and tumor accumulation in mice were studied at particular time points after tail vein injection of 0.1 mL of PBS containing **PTX/IR@BSA** nanoparticles (IR-780, 10 mg/kg) by using an IVIS imaging system (PerkinElmer) (excitation/emission, 770/820 nm). After 24 h, the mice were sacrificed and major organs and tumors were dissected for ex vivo NIR fluorescent imaging.

4.12. In Vivo Photothermal Imaging. To evaluate the effect of PTT in vivo, when the tumors reached approximately 150 mm^3 in size, **PTX/IR@BSA** nanoparticles (IR-780, 10 mg/kg) or PBS was intravenously injected into the mouse. After 24 h, the mice were irradiated with a NIR laser (808 nm, 1 W cm^{-2}) for 5 min. Thermal images were evaluated using a photothermal camera.

4.13. In Vivo ^{19}F MRI. The mice had free access to water and food until tumor size reached about 200 mm^3. The MCF-7 tumor-bearing mice were anesthetized by isoflurane, and 0.1 mL of **PTX/IR@BSA** nanoparticles was intravenously injected into the tumor-bearing mice (C_F = 0.3 mmol/kg). ^{19}F MRI was performed on the 400 MHz Bruker BioSpec MRI system. ^{1}H MRI scanning was performed using a RARE sequence (TR = 2500 ms, TE = 33 ms, FOV = 30 mm × 30 mm, 2 mm slice thickness, RARE factor = 8, matrix size = 256 × 256), and ^{19}F MRI was performed through a RARE sequence (TR = 1600 ms, TE = 3 ms, FOV = 37 mm × 37 mm, 30 mm slice thickness, matrix size = 32 × 32, 64 averages).

4.14. In Vivo Tumor Inhibition. The mice bearing MCF-7 tumors were randomly divided into six groups (G1, G2, G3, G4, G5, and G6). When the tumor volume reached about 100 mm^3, the mice in the G1 and G2 groups were intravenously injected with 0.1 mL PBS, the mice in the G3 group were intravenously injected with 0.1 mL PBS containing PTX (10 mg/kg), the mice in the G4 group were intravenously injected with 0.1 mL PBS containing Abraxane (PTX, 10 mg/kg), and the mice in the G5 and G6 groups were intravenously injected with 0.1 mL PBS containing **PTX/IR@BSA** nanoparticles (PTX, 10 mg/kg), respectively. After tail vein injection for 24 h, the tumors of the G2 and G5 groups were irradiated by NIR irradiation (808 nm, 1 W cm^{-2}, 2 min). The body weights and the tumor volumes were measured every 2 days. The tumor volume was calculated as $V = W^2 \times L/2$, in which W and L are the shortest and longest diameters of the tumor, respectively. After 22 days of treatment, the mice were sacrificed, and the major organs and tumors were dissected to detect histological changes by H&E staining.

4.15. Statistical Analysis. All experiments were repeated at least three times, and the data were presented as mean ± SD. Asterisks indicate significant differences (**$p < 0.01$, ***$p < 0.001$) by unpaired Student two-sided t test.

■ ASSOCIATED CONTENT

Supporting Information

The Supporting Information is available free of charge at https://pubs.acs.org/doi/10.1021/acsami.2c19161.

Experimental materials, synthesis and characterization of fluorinated tags and BSAs, characterization of BSA nanoparticles, cell and animal studies, and copies of ^{1}H/^{13}C/^{19}F NMR and MS spectra of compounds and fluorinated BSAs (PDF)

■ AUTHOR INFORMATION

Corresponding Authors

Zhong-Xing Jiang − *State Key Laboratory of Magnetic Resonance and Atomic and Molecular Physics, National Center for Magnetic Resonance in Wuhan, Wuhan Institute of Physics and Mathematics, Innovation Academy for Precision Measurement Science and Technology, Chinese Academy of Sciences, Wuhan 430071, China; University of Chinese Academy of Sciences, Beijing 100049, China;* orcid.org/0000-0003-2601-4366; Email: zxjiang@apm.ac.cn

Shizhen Chen − *State Key Laboratory of Magnetic Resonance and Atomic and Molecular Physics, National Center for Magnetic Resonance in Wuhan, Wuhan Institute of Physics and Mathematics, Innovation Academy for Precision Measurement Science and Technology, Chinese Academy of Sciences, Wuhan 430071, China; University of Chinese Academy of Sciences, Beijing 100049, China;* Email: chenshizhen@wipm.ac.cn

https://doi.org/10.1021/acsami.2c19161
ACS Appl. Mater. Interfaces 2023, 15, 2665−2678

Authors

Lijun Zhu − *School of Pharmaceutical Sciences, Wuhan University, Wuhan 430071, China*

Yu Li − *Innovation Academy for Precision Measurement Science and Technology, Chinese Academy of Sciences, Wuhan 430071, China*

Mou Jiang − *Innovation Academy for Precision Measurement Science and Technology, Chinese Academy of Sciences, Wuhan 430071, China*

Changsheng Ke − *School of Pharmaceutical Sciences, Wuhan University, Wuhan 430071, China*

Hanxiong Long − *School of Pharmaceutical Sciences, Wuhan University, Wuhan 430071, China*

Maosong Qiu − *Innovation Academy for Precision Measurement Science and Technology, Chinese Academy of Sciences, Wuhan 430071, China*

Lei Zhang − *Innovation Academy for Precision Measurement Science and Technology, Chinese Academy of Sciences, Wuhan 430071, China*

Chaohui Ye − *Innovation Academy for Precision Measurement Science and Technology, Chinese Academy of Sciences, Wuhan 430071, China*

Xin Zhou − *Innovation Academy for Precision Measurement Science and Technology, Chinese Academy of Sciences, Wuhan 430071, China;* orcid.org/0000-0002-5580-7907

Complete contact information is available at: https://pubs.acs.org/10.1021/acsami.2c19161

Author Contributions

Z.-X.J.: conceived and designed the project, wrote draft of the manuscript. S.C.: conceived and designed the project, provided the insights, supervised the project, and edited the paper. L.Z.: performed the synthesis and the subsequent experiments, and analyzed data. Y.L.: polished the language. M.J.: performed the ^{19}F-NMR/MRI experiments. C.K.: assisted with several cellular experiments. H.L.: assisted with several cellular experiments. M.Q.: performed the ^{19}F-NMR/MRI experiments. L.Z.: provided the insights, supervised the project, and edited the paper. C.Y.: provided the insights, supervised the project, and edited the paper. X.Z.: provided the insights, supervised the project, and edited the paper.

Notes

The authors declare no competing financial interest.

■ ACKNOWLEDGMENTS

We are thankful for the financial support from the National Key R&D Program of China (2018YFA0704000), the National Natural Science Foundation of China (22077098, 21921004, U21A20392, and 91859206), and the Knowledge Innovation Program of Wuhan -Basic Research (2022020801010137).

■ REFERENCES

(1) Kratz, F. Albumin as a Drug Carrier: Design of Prodrugs, Drug Conjugates and Nanoparticles. *J. Controlled Release* **2008**, *132*, 171−183.

(2) Elzoghby, A. O.; Samy, W. M.; Elgindy, N. A. Albumin-Based Nanoparticles as Potential Controlled Release Drug Delivery Systems. *J. Controlled Release* **2012**, *157*, 168−182.

(3) Elsadek, B.; Kratz, F. Impact of Albumin on Drug Delivery-New Applications On the Horizon. *J. Controlled Release* **2012**, *157*, 4−28.

(4) Chen, Q.; Liu, Z. Albumin Carriers for Cancer Theranostics: A Conventional Platform with New Promise. *Adv. Mater.* **2016**, *28*, 10557−10566.

(5) Hoogenboezem, E. N.; Duvall, C. L. Harnessing Albumin as a Carrier for Cancer Therapies. *Adv. Drug Delivery Rev.* **2018**, *130*, 73−89.

(6) Gradishar, W. J. Albumin-bound Paclitaxel: A Next-Generation Taxane. *Expert Opin. Pharmacother.* **2006**, *7*, 1041−1053.

(7) Hawkins, M. J.; Shiong, P. S.; Desai, N. Protein Nanoparticles as Drug Carriers in Clinical Medicine. *Adv. Drug Delivery Rev.* **2008**, *60*, 876−885.

(8) Miele, E.; Spinelli, G. P.; Miele, E.; Tomao, F.; Tomao, S. Albumin-Bound Formulation of Paclitaxel (Abraxane® ABI-007) in the Treatment of Breast Cancer. *Int. J. Nanomed.* **2009**, *4*, 99−105.

(9) Subia, B.; Kundu, S. C. Drug Loading and Release on Tumor Cells Using Silk Fibroin−Albumin Nanoparticles as Carriers. *Nanotechnology* **2013**, *24*, 035103−035113.

(10) Can, K.; Ozmen, M.; Ersoz, M. Immobilization of Albumin on Aminosilane Modified Superparamagnetic Magnetite Nanoparticles and Its Characterization. *Colloids Surf., B* **2009**, *71*, 154−159.

(11) Qi, W.-W.; Yu, H.-Y.; Guo, H.; Lou, J.; Wang, Z.-M.; Liu, P.; Minet, A. S.; Maincent, P.; Hong, X.-C.; Hu, X.-M.; Xiao, Y.-L. Doxorubicin-Loaded Glycyrrhetinic Acid Modified Recombinant Human Serum Albumin Nanoparticles for Targeting Liver Tumor Chemotherapy. *Mol. Pharmaceutics* **2015**, *12*, 675−683.

(12) Look, J.; Wilhelm, N.; Briesen, H. V.; Noske, N.; Günther, C.; Langer, K.; Gorjup, E. Ligand-Modified Human Serum Albumin Nanoparticles for Enhanced Gene Delivery. *Mol. Pharmaceutics* **2015**, *12*, 3202−3213.

(13) Li, F.; Zhao, Y.; Mao, C.; Kong, Y.; Ming, X. RGD-Modified Albumin Nanoconjugates for Targeted Delivery of a Porphyrin Photosensitizer. *Mol. Pharmaceutics* **2017**, *14*, 2793−2804.

(14) Li, W.; Wu, Y.; Li, C.; Zhu, L. Effect of (E,E)-2,4-decadienal on Side-Chain Modification, Conformation Change, and Aggregation of Bovine Serum Albumin. *Eur. J. Lipid Sci. Technol.* **2021**, *124*, 2100066−2100080.

(15) Yang, T.; Tang, Y.; Liu, L.; Lv, X.; Wang, Q.; Ke, H.; Deng, Y.; Yang, H.; Yang, X.; Liu, G.; Zhao, Y.; Chen, H. Size-Dependent Ag_2S Nanodots for Second Near-Infrared Fluorescence/Photoacoustics Imaging and Simultaneous Photothermal Therapy. *ACS Nano* **2017**, *11*, 1848−1857.

(16) Kudarha, R. R.; Sawant, K. K. Albumin Based Versatile Multifunctional Nanocarriers for Cancer Therapy: Fabrication, Surface Modification, Multimodal Therapeutics and Imaging Approaches. *Mater. Sci. Eng., C* **2017**, *81*, 607−626.

(17) Tang, Y.; Yang, T.; Wang, Q.; Lv, X.; Song, X.; Ke, H.; Gu, Z.; Huang, X.; Hu, J.; Li, Z.; Yang, P.; Yang, X.; Chen, H. Albumin-Coordinated Assembly of Clearable Platinum Nanodots for Photo-Induced Cancer Theranostics. *Biomaterials* **2018**, *154*, 248−260.

(18) Zhang, Y.; Bo, S.; Feng, T.; Qin, X.; Wan, Y.; Jiang, S.; Li, C.; Lin, J.; Wang, T.; Zhou, X.; Jiang, Z.-X.; Huang, P. A Versatile Theranostic Nanoemulsion for Architecture-Dependent Multimodal Imaging and Dually Augmented Photodynamic Therapy. *Adv. Mater.* **2019**, *31*, 1806444−1806453.

(19) Zhu, J.; Zhang, H.; Chen, K.; Li, Y.; Yang, Z.; Chen, S.; Zheng, X.; Zhou, X.; Jiang, Z.-X. Peptidic Monodisperse PEG "Comb" as Multifunctional "Add-On" Module for Imaging-Traceable and Thermo-Responsive Theranostics. *Adv. Healthcare Mater.* **2019**, *9*, 1901331−1901340.

(20) Zhang, H.; Yu, Q.; Li, Y.; Yang, Z.; Zhou, X.; Chen, S.; Jiang, Z.-X. Fluorinated Cryptophane-A and Porphyrin-Based Theranostics for Multimodal Imaging-Guided Photodynamic Therapy. *Chem. Commun.* **2020**, *56*, 3617−3620.

(21) Zhang, H.; Bo, S.; Zeng, K.; Wang, J.; Li, Y.; Yang, Z.; Zhou, X.; Chen, S.; Jiang, Z.-X. Fluorinated Porphyrin-Based Theranostics for Dual Imaging and Chemo-Photodynamic Therapy. *J. Mater. Chem. B* **2020**, *8*, 4469−4474.

(22) Chen, K.; Wu, T.; Jiang, M.; Li, A.; Peng, X.; Chen, S.; Yang, Z.; Zhou, X.; Zheng, X.; Jiang, Z.-X. Partially Fluorinated Nano-

emulsions for ^{19}F MRI-Fluorescence Dual Imaging Cell Tracking. *Colloids Surf., B* **2022**, *215*, 112493−112500.
(23) Sheng, Z.; Hu, D.; Zheng, M.; Zhao, P.; Liu, H.; Gao, D.; Gong, P.; Gao, G.; Zhang, P.; Ma, Y.; Cai, L. Smart Human Serum Albumin Indocyanine Green Nanoparticles Generated by Programmed Assembly for Dual-Modal Imaging-Guided Cancer Synergistic Phototherapy. *ACS Nano* **2014**, *8*, 12310−12322.
(24) Chen, R.; Wang, X.; Yao, X.; Zheng, X.; Wang, J.; Jiang, X. Near-IR-Triggered Photothermal/Photodynamic Dual-Modality Therapy System via Chitosan Hybrid Nanospheres. *Biomaterials* **2013**, *34*, 8314−8322.
(25) Wang, K.; Zhang, Y.; Wang, J.; Yuan, A.; Sun, M.; Wu, J.; Hu, Y. Self-Assembled IR780-Loaded Transferrin Nanoparticles as an Imaging, Targeting and PDT/PTT Agent for Cancer Therapy. *Sci. Rep.* **2016**, *6*, 27421−27432.
(26) Tang, Q.; Xiao, W.; Huang, C.; Si, W.; Shao, J.; Huang, W.; Chen, P.; Zhang, Q.; Dong, X. pH-Triggered and Enhanced Simultaneous Photodynamic and Photothermal Therapy Guided by Photoacoustic and Photothermal Imaging. *Chem. Mater.* **2017**, *29*, 5216−5224.
(27) Frangioni, J. V. In Vivo Near-Infrared Fluorescence Imaging. *Curr. Opin. Chem. Biol.* **2003**, *7*, 626−634.
(28) Luo, S.; Zhang, E.; Su, Y.; Cheng, T.; Shi, C. A Review of NIR Dyes in Cancer Targeting and Imaging. *Biomaterials* **2011**, *32*, 7127−7138.
(29) Vahrmeijer, A. L.; Hutteman, M.; Vorst, J. R.; Velde, C. J. H.; Frangioni, J. V. Image-Guided Cancer Surgery Using Near-Infrared Fluorescence. *Nat. Rev. Clin. Oncol.* **2013**, *10*, 507−518.
(30) Hong, G.; Antaris, A. L.; Dai, H. Near-Infrared Fuorophores for Biomedical Imaging. *Nat. Biomed. Eng.* **2017**, *1*, 10−31.
(31) Ruiz-Cabello, J.; Barnett, B. P.; Bottomley, P. A.; Bulte, J. W. Fluorine (^{19}F) MRS and MRI in Biomedicine. *NMR Biomed.* **2011**, *24*, 114−129.
(32) Ahrens, E. T.; Jia, Z. In Vivo MRI Cell Tracking Using Perfluorocarbon Probes and Fluorine-19 Detection. *NMR Biomed.* **2013**, *26*, 860−871.
(33) Tirotta, I.; Dichiarante, V.; Pigliacelli, C.; Cavallo, G.; Terraneo, G.; Bombelli, F. B.; Metrangolo, P.; Resnati, G. ^{19}F Magnetic Resonance Imaging (MRI): From Design of Materials to Clinical Applications. *Chem. Rev.* **2015**, *115*, 1106−1129.
(34) Wu, L.; Liu, F.; Liu, S.; Xu, X.; Liu, Z.; Sun, X. Perfluorocarbons-Based ^{19}F Magnetic Resonance Imaging in Biomedicine. *Int. J. Nanomed.* **2020**, *15*, 7377−7395.
(35) Lin, H.; Tang, X.; Li, A.; Gao, J. Activatable ^{19}F MRI Nanoprobes for Visualization of Biological Targets in Living Subjects. *Adv. Mater.* **2021**, *33*, 2005657−2005665.
(36) Wu, T.; Li, A.; Chen, K.; Peng, X.; Zhang, J.; Jiang, M.; Chen, S.; Zheng, X.; Zhou, X.; Jiang, Z.-X. Perfluoro-tert-butanol: A Cornerstone for High Performance Fluorine-19 Magnetic Resonance Imaging. *Chem. Commun.* **2021**, *57*, 7743−7757.
(37) Crich, S. G.; Terreno, E.; Aime, S. Nano-Sized and Other Improved Reporters for Magnetic Resonance Imaging of Angiogenesis. *Adv. Drug Delivery Rev.* **2017**, *119*, 61−72.
(38) Ren, H.; Liu, J.; Su, F.; Ge, S.; Yuan, A.; Dai, W.; Wu, J.; Hu, Y. Relighting Photosensitizers by Synergistic Integration of Albumin and Perfluorocarbon for Enhanced Photodynamic Therapy. *ACS Appl. Mater. Interfaces* **2017**, *9*, 3463−3473.
(39) Zhou, Z.; Zhang, B.; Zai, W.; Kang, L.; Yuan, A.; Hu, Y.; Wu, J. Perfluorocarbon Nanoparticle-Mediated Platelet Inhibition Promotes Intratumoral Infiltration of T cells and Boosts Immunotherapy. *Proc. Natl. Acad. Sci. U. S. A.* **2019**, *116*, 11972−11977.
(40) Mehta, V. D.; Kulkarni, P. V.; Mason, R. P.; Constantinescu, A.; Antich, P. P. Fluorinated Proteins as Potential ^{19}F Magnetic Resonance Imaging and Spectroscopy Agents. *Bioconjugate Chem.* **1994**, *5*, 257−261.
(41) Chubarov, A. S.; Shakirov, M. M.; Koptyug, I. V.; Sagdeev, R. Z.; Knorre, D. G.; Godovikova, T. S. Synthesis and Characterization of Fluorinated Homocysteine Derivatives as Potential Molecular Probes for ^{19}F Magnetic Resonance Spectroscopy and Imaging. *Bioorg. Med. Chem. Lett.* **2011**, *21*, 4050−4053.
(42) Chubarov, A. S.; Zakharova, O. D.; Koval, O. A.; Romaschenko, A. V.; Akulov, A. E.; Zavjalov, E. L.; Razumov, I. A.; Koptyug, I. V.; Knorre, D. G.; Godovikova, T. S. Design of Protein Homocystamides with Enhanced Tumor Uptake Properties for ^{19}F Magnetic Resonance Imaging. *Bioorg. Med. Chem. Lett.* **2015**, *23*, 6943−6954.
(43) Lisitskiy, V. A.; Khan, H.; Popova, T. V.; Chubarov, A. S.; Zakharova, O. D.; Akulov, A. E.; Shevelev, O. B.; Zavjalov, E. L.; Koptyug, I. V.; Moshkin, M. P.; Silnikov, V. N.; Ahmad, S.; Godovikova, T. S. Multifunctional Human Serum Albumin-Therapeutic Nucleotide Conjugate with Redox and pH-Sensitive Drug Release Mechanism for Cancer Theranostics. *Bioorg. Med. Chem. Lett.* **2017**, *27*, 3925−3930.
(44) Yue, X.; Feng, Y.; Yu, Y. Synthesis and Characterization of Fluorinated Conjugates of Albumin. *J. Fluorine Chem.* **2013**, *152*, 173−181.
(45) Cao, B.; Endsley, S.; Andersen, N. H. ^{19}F NMR Studies of Tryptophan/Serum Albumin Binding. *Bioorg. Med. Chem.* **2003**, *11*, 69−75.
(46) Kitamura, K.; Kume, M.; Yamamoto, M.; Takegami, S.; Kitade, T. ^{19}F NMR Spectroscopic Study on the Binding of Triflupromazine to Bovine and Human Serum Albumins. *J. Pharm. Biomed. Anal.* **2004**, *36*, 411−414.
(47) Michelena, O.; Padro, D.; Carrillo-Carrio'n, C.; del Pino, P.; Blanco, J.; Arnaiz, B.; Parak, W. J.; Carril, M. Novel Fluorinated Ligands for Gold Nanoparticle Labeling with Applications in ^{19}F-MRI. *Chem. Commun.* **2017**, *53*, 2447−2450.
(48) Chaubey, B.; Pal, S. Binding Interaction of Organofluorine−Serum Albumin: A Comparative Ligand-Detected ^{19}F NMR Analysis. *J. Phys. Chem. B* **2018**, *122*, 9409−9418.
(49) Arango, J. M.; Padro, D.; Blanco, J.; Lopez-Fernandez, S.; Castellnou, P.; Villa-Valverde, P.; Ruiz-Cabello, J.; Martin, A.; Carril, M. Fluorine Labeling of Nanoparticles and In Vivo ^{19}F Magnetic Resonance Imaging. *ACS Appl. Mater. Interfaces* **2021**, *13*, 12941−12949.
(50) Zhang, P.; Huang, H.; Banerjee, S.; Clarkson, G. J.; Ge, C.; Imberti, C.; Sadler, P. J. Nucleus-Targeted Organoiridium-Albumin Conjugate for Photodynamic Cancer Therapy. *Angew. Chem., Int. Ed.* **2019**, *58*, 2350−2354.
(51) Zhang, H.; Li, X.; Shi, Q.; Li, Y.; Xia, G.; Chen, L.; Yang, Z.; Jiang, Z.-X. Highly Efficient Synthesis of Monodisperse Poly(ethylene glycols) and Derivatives Through Macrocyclization of Oligo(ethylene glycols). *Angew. Chem., Int. Ed.* **2015**, *54*, 3763−3767.
(52) Li, Y.; Qiu, X.; Jiang, Z.-X. Macrocyclic Sulfates as Versatile Building Blocks in the Synthesis of Monodisperse Poly(ethylene glycol)s and Monofunctionalized Derivatives. *Org. Process Res. Dev.* **2015**, *19*, 800−805.
(53) Li, Y.; Wang, X.; Chen, Y.; Yang, Z.; Jiang, Z.-X. Monodisperse Polyethylene Glycols "Brushes" with Enhanced Lipophilicity, Thermo and Plasma Stability. *Chem. Commun.* **2019**, *55*, 1895−1898.
(54) Riener, C. K.; Kada, G.; Gruber, H. J. Quick Measurement of Protein Sulfhydryls with Ellman's Reagent and with 4,4'-Dithiodipyridine. *Anal. Bioanal. Chem.* **2002**, *373*, 266−276.
(55) Wang, J.; Deng, T.; Liu, Y.; Chen, K.; Yang, Z.; Jiang, Z.-X. Monodisperse and Polydisperse PEGylation of Peptides and Proteins: A Comparative Study. *Biomacromolecules* **2020**, *21*, 3134−3139.
(56) Na, H. B.; Song, I. C.; Hyeon, T. Inorganic Nanoparticles for MRI Contrast Agents. *Adv. Mater.* **2009**, *21*, 2133−2148.
(57) Gong, T.; Tan, T.; Zhang, P.; Li, H.; Deng, C.; Huang, Y.; Gong, T.; Zhang, Z. Palmitic Acid-Modified Bovine Serum Albumin Nanoparticles Target Scavenger Receptor-A on Activated Macrophages to Treat Rheumatoid Arthritis. *Biomaterials* **2020**, *258*, 120296−120319.
(58) Qiu, M.; Tang, Y.; Chen, J.; Muriphc, R.; Ye, Z.; Huang, C.; Evansc, J.; Henskeb, E. P.; Xu, Q. Lung-Selective mRNA Delivery of Synthetic Lipid Nanoparticles for the Treatment of Pulmonary Lymphangioleiomyomatosis. *Proc. Natl. Acad. Sci. U. S. A.* **2022**, *119*, No. e2116271119.

https://doi.org/10.1021/acsami.2c19161
ACS Appl. Mater. Interfaces 2023, 15, 2665−2678

(59) Blanco, E.; Shen, H.; Ferrari, M. Principles of Nanoparticle Design for Overcoming Biological Barriers to Drug Delivery. *Nat. Biotechnol.* **2015**, *33*, 914−925.

https://doi.org/10.1021/acsami.2c19161
ACS Appl. Mater. Interfaces 2023, 15, 2665−2678